

Contents lists available at ScienceDirect

Chemical Engineering Journal

journal homepage: www.elsevier.com/locate/cej





Cellular-level insight into biointerface: From surface charge modulation to boosted photocatalytic oxidative disinfection

Zan Zhu ^a, Liang Bao ^b, Dmitry Pestov ^c, Ping Xu ^b, Wei-Ning Wang ^{a,*}

- ^a Department of Mechanical and Nuclear Engineering, Virginia Commonwealth University, Richmond, VA 23219. USA
- ^b Philips Institute for Oral Health Research, Virginia Commonwealth University, Richmond, VA 23298, USA
- ^c Nanomaterials Characterization Center, Virginia Commonwealth University, Richmond, VA 23284, USA

ARTICLE INFO

Keywords: Microorganisms Sterilization Heterojunction Photocatalysis Adhesion forces

ABSTRACT

Photocatalytic oxidative disinfection (POD) towards pathogenic bacteria has become a popular approach in public health due to its environmentally friendly antimicrobial capabilities. However, this approach is still limited by inherent fast electron-hole recombination within photocatalysts and poor interactions between bacterial cells and photogenerated reactive oxygen species (ROS) at the biointerface. Particularly, those ROS with extremely short migration distances cannot reach the bacterial cells before they deteriorate into less potent or neutral species, resulting in reduced antibacterial activities. By far, these phenomena are still poorly understood. Inspired by the fact that bacterial cells are negatively charged, we rationally designed a photocatalyst (i.e., g-C₃N₄/MIL-125-NH₂) by coating a layer of positively charged quaternary ammonium compound (QAC) polymer onto the surface to enhance its affinity towards bacterial cells via electrostatic attractions. This surfacemodulated photocatalyst is denoted as QAC@g-C₃N₄/MIL-125-NH₂. The visualization and quantification of the electrostatic interactions between the bacterial cells and the QAC@g-C₃N₄/MIL-125-NH₂ photocatalyst were conducted using a confocal laser scanning microscope and atomic force microscope, respectively. The results showed that the positively charged QAC layer did promote the bacteria-photocatalyst contact via electrostatic attractions. Due to the cooperative effects of bacterial cell adhesion and ROS generation, the POD performance of the photocatalyst is significantly enhanced. Notably, the photocatalyst achieves 3.20 logs of inactivation efficiency for Staphylococcus epidermidis within 60 min under visible light irradiation. This work provides insights into a mechanistic understanding of bacterial adhesion and disinfection at the biointerface and sheds light on rational photocatalyst design with surface charge modulation for antibacterial applications.

1. Introduction

The ongoing COVID-19 pandemic, caused by a new human coronavirus (SARS-CoV-2), has posed a severe threat to human health [1–3]. Besides SARS-CoV-2, many other pathogenic microorganisms are also devastating to humans. Pathogenic bacteria, for instance, infect millions of people and kill over one million people every year, which results in a heavy burden on the social economy and public health [4–6]. Pathogenic bacteria are typically transmitted *via* direct and indirect modes. In direct transmission, the pathogenic bacteria are transferred from a reservoir to a susceptible host by direct contact or droplet spread [7]. By indirect transmission, people are infected by the bio-contaminants in the environment, such as airborne particles, food, water, and fomites (contaminated surfaces) [3,8,9]. Converging evidence shows that

environmental biocontamination will result in an increased risk of secondary transmission [10]. Therefore, efficient disinfection in the environment is essential to decrease the spread of pathogenic bacterial transmission and thus assure the safety of public health [8,11–16].

Photocatalytic oxidative disinfection (POD) is receiving considerable attention as it uses light to generate various reactive oxygen species (ROS) to eradicate pathogenic bacteria [15–19]. To be specific, the light in the POD system can excite the charge carriers (e.g., electrons) on the surface of the photocatalyst which then react with surrounding water or oxygen molecules to produce reactive ROS. ¹⁴ Superoxide (\cdot O₂), hydroxyl radical (OH), hydrogen peroxide (+2O₂), and singlet oxygen (+1O₂) are commonly known ROS, which cause extensive damage to most macromolecules in bacterial cells including protein, DNA, and lipids [14,17,20–31]. To improve the POD performance of photocatalysts,

E-mail address: wnwang@vcu.edu (W.-N. Wang).

^{*} Corresponding author.

extensive research efforts have been put into the design of photocatalysts to address a major issue in photocatalysis, which is the inherent fast electron-hole recombination rates [32-35]. Among various strategies, constructing a heterojunction structure by combining two semiconductors with proper band alignments is a popular approach to promote charge transfer and thus improve ROS generation [17,33,36,37]. Some examples of such photocatalysts are g-C₃N₄/TiO₂, g-C₃N₄/metal-organic framework (MOF), and TiO₂/Cu₂O [32,35,38]. However, most such photocatalysts demonstrated limited improvements in the POD performance probably because the photogenerated ROS with short lifespans at the catalyst surface cannot immediately reach the bacterial cells before they degrade into less potent species, which makes the bactericidal efficacy depends only on the overall ROS concentration in the system [31]. Due to the complex reactions in the POD, the dynamic evolution of ROS diffusion and the cellular-level understanding of interactions between bacterial cells and ROS, especially for those with extremely short lifespans, are still lacking and not considered in the materials design. These factors are important because the utilization of ROS affects bactericidal efficacy profoundly [39,40].

In a POD system, ROS are generated on the surface of the photocatalyst, and they typically have short half-life times $(t_{1/2})$ and migration distances (λ) [31,41]. Specifically, OH, O_2 , 1O_2 , and H_2O_2 have half-life times of 1 μ s, 1–4 μ s, 1–4 μ s, and 1 ms with migration distances of 1 nm, 30 nm, 30 nm, and 1 µm, respectively [42]. For example, OH radicals only affect bacterial cells located a few nanometers ($\lambda_{OH}=1$ nm) from their generation sites. Given the extremely short half-life time $(t_{1/2} = 1 \mu s)$, OH species are unlikely to reach cells and cause damage to biomolecules in most cases [28]. Even though OH is 100-fold more potent than H₂O₂ and O₂, the antimicrobial capability is not fully utilized, which limits the overall photocatalytic bactericidal efficacy [28,43]. Moreover, the movement of bacterial cells in the aqueous POD system is generally unpredictable [44]. The poor affinity of bacterial cells to the photocatalyst surface will result in slow photocatalytic disinfection rates [39]. For example, bacterial cells are negatively charged due to the abundant carboxylic and phosphate groups in the cell wall [45-47]. However, most metal oxide-based photocatalysts (e.g., TiO₂) also carry negative charges in neutral pH due to the hydroxide anions (OHT) on the surface [47]. The same negative charges create electrostatic repulsion at the biointerface, leading to a decreased bacterial cell adhesion on the photocatalyst. In this case, photocatalytic disinfection depends only on ROS diffusion and penetration into bacterial cells [48]. Therefore, to further boost the photocatalytic performance, shortening the distance between bacterial cells and photocatalyst is a reasonable approach. But how can we promote the bacteria-photocatalyst contact in the POD system?

The well-established extended Derjaguin-Landau-Verwey-Overbeek (XDLVO) theory can be used to investigate the interactions between a bacterial cell and a surface [49,50]. The total adhesion force (F_{adh}) is expressed as follows: [49].

$$F_{adh} = F_{vdW} + F_e + F_{AB} \tag{1}$$

where F_{vdW} is the classical van der Waals force, F_e is the electrostatic force, and F_{AB} is the acid-base (AB) interaction force. If F_{adh} has an overall positive value, namely, the attractive forces overweigh repulsive forces, the contact between bacterial cells and material surface proceeds, and *vice versa*. F_{vdW} is generally attractive regardless of the types of bacteria and materials. F_{AB} can be either attractive or repulsive depending on the environment, bacteria, and the surface chemistry of materials. But F_{AB} is only effective in a short-range (i.e., within 1 nm) due to the electron acceptor/electron donor interactions between polar moieties in polar media (e.g., water) [49,51]. Therefore, the interaction in a longer range is governed by the overall effects of F_{vdW} and F_e . Fortunately, in the natural water system, almost all bacteria are negatively charged. This gives the chance to modulate a positively charged surface to attract bacterial cells with electrostatic effects [45–47], which

is expected to endow the photocatalyst with more efficient photocatalytic antibacterial activities [39,52].

In this study, we aim to quantify the dynamic interactions between bacterial cells and the photocatalyst at a cellular level and to further unravel the role of these interactions in the enhancement of POD performance. To achieve these goals, we designed a hybrid photocatalyst by coating a layer of positively charged quaternary ammonium compound (QAC) polymer onto the surface of g-C₃N₄/MIL-125-NH₂ composite. The final product is termed "QAC@g-C3N4/MIL-125-NH2". The bare photocatalyst g-C₃N₄/MIL-125-NH₂ is composed of two components: g-C₃N₄ is a two-dimension (2D) material comprising small sheets with wrinkles, while MIL-125-NH2 refers to a titanium (Ti)-based MOF, a class of highly porous materials constructed by metal ions and organic ligands. Both g-C₃N₄ and MIL-125-NH₂ are popular visible-light responsive photocatalysts [18,34,53]. The rational design of g-C₃N₄/MIL-125-NH₂ heterojunction promotes charge separation and transfer, thus, improving the photocatalytic activity [32,54]. Moreover, the layer of positively charged QAC polymer coated on the surface is another critical component. Not only because the QAC, a well-known broad-spectrum bactericidal agent, can destroy bacterial membranes via electrostatic interaction [55,56], but more importantly, this positively charged layer can attract the negatively charged bacterial cells to the surface and shorten the distance between the ROS and bacterial cells, which will help make full use of ROS during photocatalysis reactions. As expected, compared to the bare photocatalyst, QAC@g-C3N4/MIL-125-NH2 demonstrated significantly improved photocatalytic antibacterial performance, achieving 3.20 log inactivation efficiency in 60 min for a representative bacterium, S. epidermidis. Systematic material characterization and biological experiments were carried out to reveal the cooperative photocatalytic antibacterial behaviors caused by the positively charged QAC layer and the g-C $_3N_4/MIL$ -125-NH $_2$ heterojunction. Particularly, we used an atomic force microscope (AFM), a powerful tool to quantify the force-distance relationships between QAC@g-C3N4/MIL-125-NH2 and bacterial cells. A remarkable enhancement in adhesion force of 972 pN was observed between QAC@g-C3N4/MIL-125-NH2 modified cantilever tip and bacteria, while only 115 pN adhesion force was detected between unmodified reference tip and bacteria. The results again confirm that positive charge modulation on the MOF-based catalyst facilitates bacterial adhesion on the photocatalyst surface. The outcomes of this work provide insights into a mechanistic understanding of bacterial adhesion and disinfection at the biointerface and shed light on rational photocatalyst design with surface charge modulation for antibacterial applications.

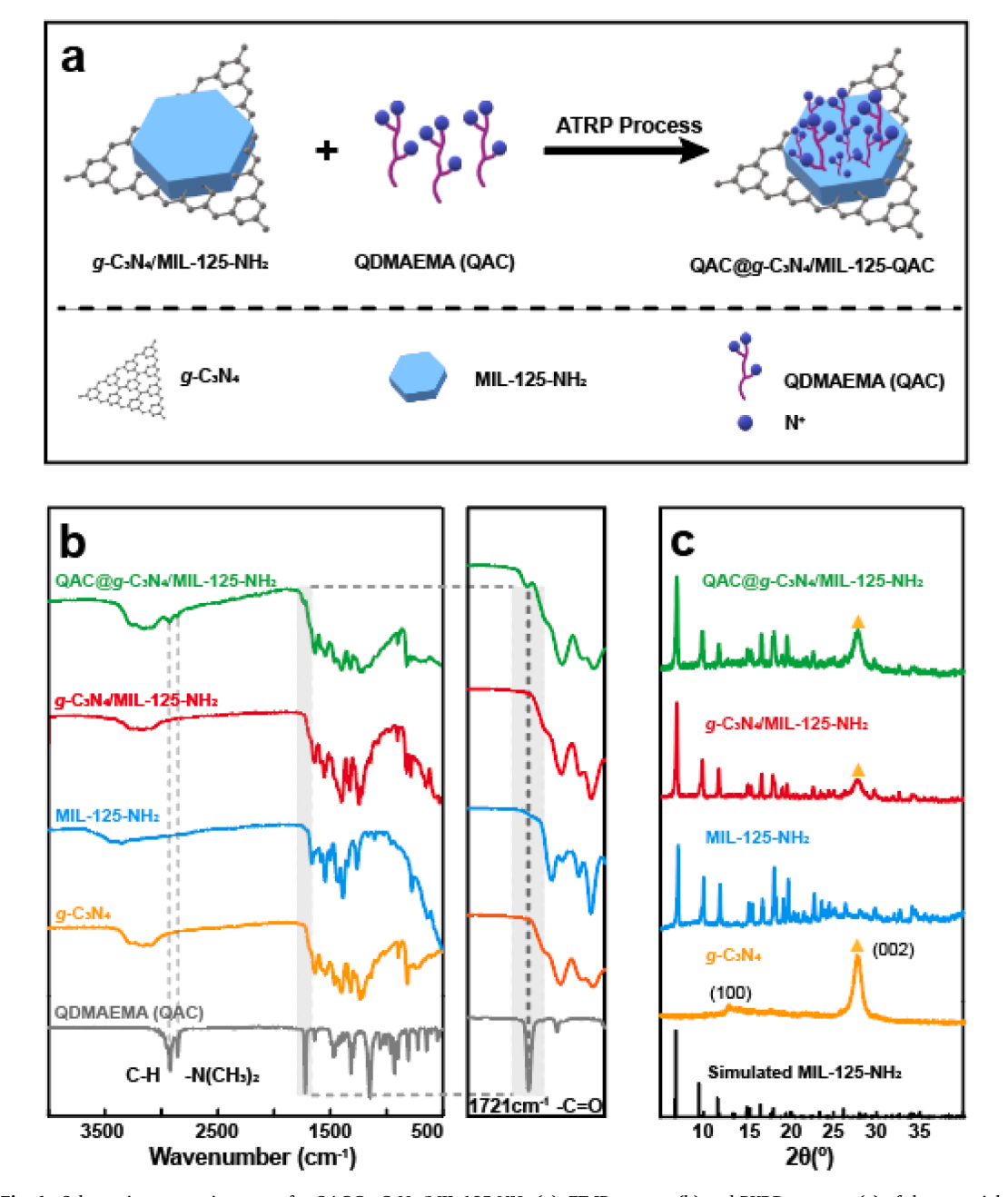
2. Experimental

2.1. Preparation of photocatalysts

The bare photocatalyst $g\text{-}C_3N_4/\text{MIL-}125\text{-}NH_2$ is fabricated via a solvothermal method, where the pre-synthesized $g\text{-}C_3N_4$ was suspended in the precursor of MIL-125-NH₂. The mixture was then subjected to heat treatment in a 100 mL Teflon-lined steel autoclave reactor at 150 °C for 15 h [33]. For QAC coating, the monomer 2-(dimethyl decyl ammonium) ethyl methacrylate (QDMAEMA) was polymerized and grafted on the surface of $g\text{-}C_3N_4/\text{MIL-}125\text{-}NH_2$ through the classical atomic transfer radical polymerization (ATRP) approach [45] to obtain the final product, which is denoted as QAC@ $g\text{-}C_3N_4/\text{MIL-}125\text{-}NH_2$. The schematic preparation route for QAC@ $g\text{-}C_3N_4/\text{MIL-}125\text{-}NH_2$ is shown in Fig. 1a. The details on the chemical information and material synthesis can be seen in Supporting information 1 (SI 1).

2.2. Material characterization

The chemical functional groups were examined by a Fourier transform infrared (FT-IR) spectrometer (Nicolet iS50, Thermo Scientific). The crystallinity of the materials was determined by powder X-ray



 $\textbf{Fig. 1.} \ \ \textbf{Schematic preparation route for QAC@g-C}_{3}N_{4}/\text{MIL-125-NH}_{2} \ (a); \ \textbf{FT-IR spectra (b) and PXRD patterns (c) of the materials.}$

diffraction (PXRD, PANalytical X'Pert Pro MPD). Morphologies of the materials were observed by scanning electron microscopy (SEM, Su-70, Hitachi) and transmission electron microscopy (TEM, JEM-F200, JOEL). Element mapping was conducted using energy disperse spectroscopy (EDS). The N2 adsorption-desorption experiments were carried out using Autosorb iQ (Quantachrome Instrument). The surface area was calculated based on the Brunauer-Emmett-Teller (BET) theory [57]. The desorption data were used to determine the pore-size distribution by using the Barret-Joyner-Halender (BJH) method [58]. Thermal stability and components of the samples were determined by thermogravimetric analysis (TGA) (TGA Q500, TA Instruments) under a nitrogen flow environment. The optical properties of the samples were investigated by a UV-visible (UV-vis) spectrometer (Evolution 220, ThermoFisher). The surface charge of the materials was examined by a zeta potential analyzer (Zetasizer Nano ZS, Malvern Instruments Ltd.). The electronic state of the elements within the materials was analyzed by X-ray photoelectron spectroscopy (XPS, PHI VersaProbe III Scanning XPS Microprobe). The fluorescence images were obtained by the Zeiss Axiovert 200 M fluorescence microscope. Water contact angles (WCA) were measured by a goniometer (OCA 15, DataPhysics).

2.3. Photocatalytic disinfection

Staphylococcus epidermidis ATCC 14,990 (S. epidermidis) was used as the model bacterium. S. epidermidis cells were cultured in a medium containing 5 g peptone/L and 3 g meat extract/L at 37 °C for 18 h to yield a cell concentration of $\sim 10^9$ CFU/mL [59]. Then, S. epidermidis was washed with the sterilized phosphate-buffered saline (PBS) (pH = 7.4) by centrifugation (4000 rpm for 10 min). The final bacterial concentration for bactericidal experiments was adjusted to $\sim 10^7$ CFU/mL using the PBS buffer.

Typically, 1.5 mg photocatalyst was added into a quartz cuvette containing a 3 mL bacterial solution ($\sim 10^7$ CFU/mL). The bacterial cells and photocatalysts were sufficiently mixed at room temperature and

irradiated under the simulated solar light at an intensity of 100 mW/cm². The Xe lamp (450 W, Newport Corporation) was equipped with a water filter to remove unwanted IR light, as well as an ultraviolet (UV) cut-off filter (390 nm, Edmund Optics) to limit the lethal UV exposure to the bacterial cells. After exposure to the light at various periods (15–60 min), a 100 μ L mixture was pipetted out. The bacterial concentration was determined by the standard plate counting method. The agar plates containing the collected bacterial cells with a series of dilutions were incubated at 37 °C overnight for enumeration. The control experiments were conducted without light irradiation in the same situations. The bacterial inactivation efficiency (E) was calculated by the following equation:

$$E = \log \frac{C}{C_0} \tag{2}$$

where C and C_0 are the bacterial CFU of the samples taken at a specific time and before the light irradiation, respectively.

2.4. ROS determination and measurements

The species of ROS were determined by well-established scavenger tests [60], where various trapping agents were added to the photoreactor during the reaction. Specifically, isopropyl alcohol, catalase, and p-benzoquinone were used as the scavengers for \bullet OH, H_2O_2 , and $\bullet O_2^-$, respectively [60,61]. To exclude the toxicity effects of the scavenger agents (e.g., p-benzoquinone) on the bacterial cells, the photocatalytic experiments were performed in the same situation but with a replacement of Rhodamine B dye [62]. Details of ROS determination and quantification are provided in SI 2.

2.5. Bacterial staining

The bacterial cells were visualized by a fluorescence microscope. Specifically, 1 mL bacterial cell suspension was centrifuged and resuspended in 100 μ L of PBS solution, which was subsequently stained by a live/dead staining kit (Molecular Probes, Invitrogen). Bacterial cells with intact cell membranes (live) were stained by SYTO 9 which emits green fluorescence, whereas the dead bacterial cells with damaged membranes were stained by propidium iodide (PI), which emits red fluorescence [45,63].

2.6. AFM measurements

2.6.1. Bacterial immobilization

Bacterial immobilization is important as a small movement during AFM imaging in a fluid will lead to unstable and even incorrect results [64]. To firmly fix the bacterial cells on the substrate, the following treatments were applied [39]. Specifically, the overnight cultured bacterial cells were washed three times with PBS with centrifugation at 4000 rpm for 10 min. Then, the collected pellets were resuspended in a 1 mL filter-sterilized PBS solution and treated with 1-ethyl-3-(3dimethylaminopropyl) carbodiimide (EDC, 1 mg/mL) and *N*-hydroxysuccinimide (NHS, 2 mg/mL) for 10 min. After EDC and NHS treatments, the carboxyl groups on the bacterial surface were converted into amine-active succinimidyl esters. A drop of the above bacterial suspension (40 μ L) was placed on a poly-L-lysine treated glass slide for 20 min and rinsed with PBS solution sufficiently to remove the loosely attached bacterial cells. The remaining bacterial cells were immobilized on the poly-L-lysine coated glass slide.

2.6.2. AFM force-curve measurement in fluid

Force-curve measurements were carried out at room temperature in PBS solution, using a Dimension Icon AFM (Bruker Corporation) with the peak force tapping mode (PeakForce-Quantitative Nano-Mechanics). A tip of SCANAYST-FLUID+ (Bruker) with a spring constant of $\sim 0.7~\rm N/$

m was used. Before each measurement, the spring constant and the deflection sensitivity were calibrated using the "touch calibration" method. The trig threshold force (peak force setpoint) was set to 2.0 nN to get enough indentation on the bacterial surface. The scan rate was adjusted to 1 Hz, and the peak force amplitude was set to 150 nm to obtain stable force curves. The images were recorded at 128 pixels \times 128 pixels with a driving frequency of 1 kHz. Data processing was performed using the commercial Nanoscope Analysis 2.0 software (Bruker AXS Corporation). Sixteen pairs of "approach" and "retract" data were extracted and averaged from the force volume image for further analysis.

3. Results and discussion

3.1. Materials characterization

The representative samples were first subjected to detailed characterization. As shown in Fig. 1b, characteristic vibrational bands from both g-C₃N₄ and MIL-125-NH₂ can be found in the FT-IR spectrum of QAC@g-C₃N₄/MIL-125-NH₂. Particularly, a new peak at 1721 cm⁻¹, which is attributed to the C=O stretching vibration of easter groups from QAC, is observed in QAC@g-C₃N₄/MIL-125-NH₂ (see Fig. 1b, grey area); besides, two additional peaks at 2822 cm⁻¹ and 2770 cm⁻¹ are also found in QAC@g-C₃N₄/MIL-125-NH₂, which are assigned to the -N (CH₃)₂ symmetric and asymmetric vibrations of QAC, respectively [45,65]. Therefore, it can be concluded that the QAC has been successfully grafted onto the g-C₃N₄/MIL-125-NH₂ heterostructure via the ATRP approach, g-C₃N₄ and MIL-125-NH₂ in the composites were also identified by PXRD analysis. For example, MIL-125-NH2 in QAC@g-C₃N₄/MIL-125-NH₂ was confirmed by several characteristic peaks at 6.8° , 9.5° , and 11.6° , which are ascribed to the (101), (200), and (211) crystal planes, respectively [66]. The presence of g-C3N4 is also evidenced by its main PXRD peak at 11.1° and 27.7°, corresponding to its (100) and (002) planes, respectively (see Fig. 1c) [39].

The morphologies of g-C₃N₄/MIL-125-NH₂ and QAC@g-C₃N₄/MIL-125-NH₂ were examined by TEM. As shown in Fig. 2a, the plate-like crystals of MIL-125-NH2 covered by some g-C3N4 nanosheets were embedded in the wrinkling lamellar structure, which indicates a close contact between MIL-125-NH2 and g-C3N4. The interactions between g-C₃N₄ and MIL-125-NH₂ in the heterojunction are mainly dominated by van der Waals forces because both g-C₃N₄ and 1,4-benzene dicarboxylic acid ligands in MIL-125-NH $_2$ are π -rich structures, which leads to the strong π - π interactions through unsaturated (poly)cyclic molecules [33,67]. This heterogeneous structure of g-C₃N₄/MIL-125-NH₂ photocatalyst is similar to the previously reported g-C₃N₄/MOF heterojunction [33]. Furthermore, a clear lattice fringe of g-C₃N₄ nanosheets with a dspacing of 0.328 nm was determined in the high resolution (HR)-TEM image of g-C₃N₄/MIL-125-NH₂ (see Fig. 2b), which is attributed to the (002) lattice plane of g-C₃N₄. It should be noted that MIL-125-NH₂ is a crystalline polymer, which is extremely sensitive to high intensity electron beams and its structure can be easily damaged during HR-TEM imaging [68]. To avoid the damage of the structure of MIL-125-NH2, a low electron voltage of 80 keV was used, which resulted in the image of dark crystals instead of the fringe lattice (see Fig. 2(a, b)). Based on the XRD, FT-IR, and TEM analysis, it can be concluded that the heterojunction between g-C₃N₄ and MIL-125-NH₂ is constructed [33].

To further confirm the presence of QAC polymer, an EDS mapping analysis was conducted. The uniform distribution of C, Ti, and Br is observed in Fig. 2(d-f), where Br is from the initiator molecule (i.e., 2-bromoisobutyryl bromide) and 1-bromodecane (CH₃(CH₂)₈CH₂Br) quaternized QAC polymers during the ATRP process. This again indicates that the QAC polymer was successfully coated on the surface of the heterojunction. Based on the TGA analysis, the weight percentage of this polymeric QAC layer is determined to be 17.4 % (see SI 4). It should be noted that the surface hydrophobicity of g-C₃N₄/MIL-125-NH₂ was significantly changed as well because the grafted polymeric QAC layer

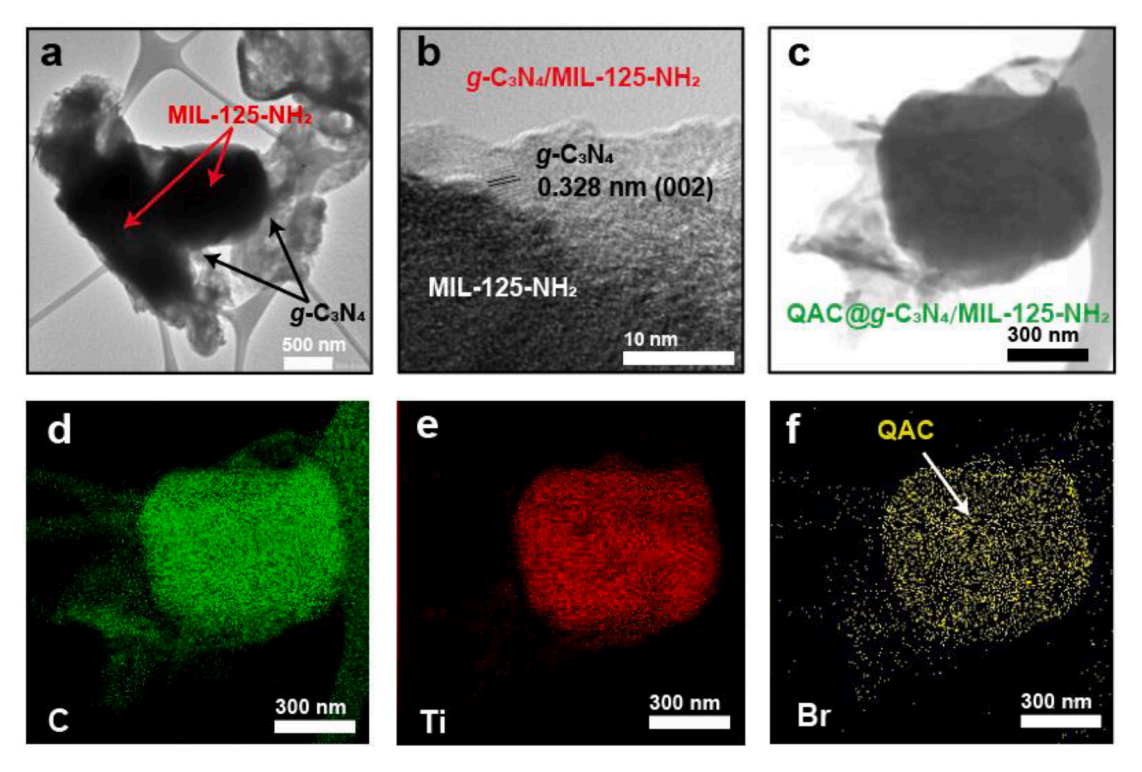


Fig. 2. TEM (a) and HR-TEM (b) images of g-C₃N₄/MIL-125-NH₂; (c) TEM image of QAC@g-C₃N₄/MIL-125-NH₂; (d-f) EDS mapping images of QAC@g-C₃N₄/MIL-125-NH₂.

contains a long alkyl chain length (n = 8) [65]. As demonstrated in the insects in Fig. S3(c, d), QAC@g-C_3N_4/MIL-125-NH_2 exhibited a hydrophobic surface with a WCA of 153°, while g-C_3N_4/MIL-125-NH_2 showed a hydrophilic surface with a WCA of 0°. All the above results once again confirmed the successful QAC coating on the g-C_3N_4/MIL-125-NH_2 photocatalyst.

3.2. POD performance

The bacterial inactivation experiments were carried out in PBS solution (pH = 7.4) under visible light irradiation. S. epidermidis is selected as a representative bacterium for POD tests throughout this study. The UV and IR lights from the Xe lamp were removed (see details in Section **2.3**) to ensure the safety of bacteria [69]. The blank experiment with the light on confirmed the negligible bactericidal activity, compared to the dark control group (S. epidermidis in the dark without photocatalyst, see Fig. 3). The bare photocatalyst g- C_3N_4/MIL -125- NH_2 also exhibited an unnoticeable reduction of bacterial cells in the dark, whereas it reaches a 1.5 logs reduction of S. epidermidis under the light irradiation, suggesting the bactericidal activity is mainly due to the photogenerated ROS in the solution rather than the toxicity of the catalyst itself. Interestingly, for QAC@g-C₃N₄/MIL-125-NH₂ in the dark, it can achieve a 1.54 logs reduction of S. epidermis via the contact-killing mechanism due to the QAC coating [70]. When the light is further applied, a significantly boosted photocatalytic bactericidal efficiency of 3.2 logs reduction of S. epidermis was obtained. Therefore, at the biointerface, the photogenerated ROS and the positively charged QAC layer demonstrate cooperative antibacterial behaviors, which significantly improve the overall bactericidal activities. To reveal the mechanism of photocatalytic disinfection using QAC@g-C₃N₄/MIL-125-NH₂, an in-depth analysis is carried out from the following aspects. (i) photocatalytic performance of g-C₃N₄/MIL-125-NH₂; (ii) charge effects of QAC; and (iii) bacteria-photocatalyst interactions.

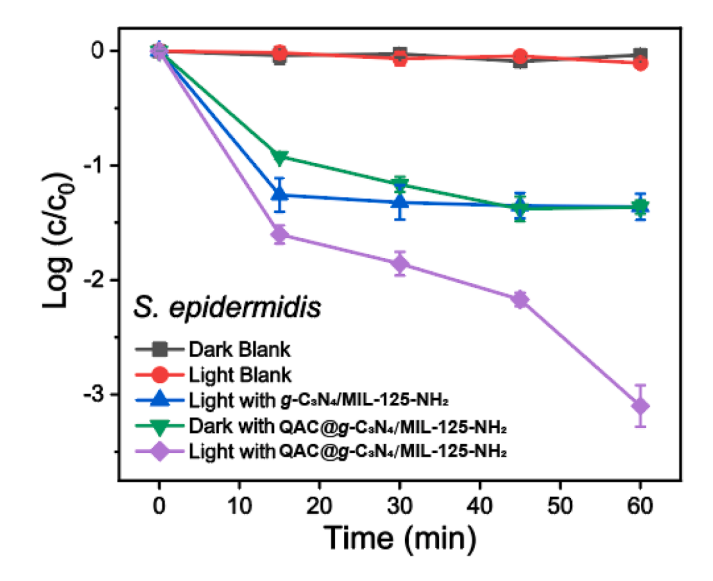


Fig. 3. Time-course of bactericidal activities for *S. epidermidis* under different conditions.

3.3. Photocatalytic performance of $g-C_3N_4/MIL-125-NH_2$

When used alone, either $g\text{-}C_3N_4$ or MIL-125-NH $_2$ suffers from poor photocatalytic activity because of the fast recombination rate of electron-hole pairs [34]. The formation of semiconductor heterojunctions with an appropriate band alignment is a viable approach to boost the charge separation and transfer kinetics, which in turn gives to an enhanced photocatalytic performance of the catalyst [33]. In this study, $g\text{-}C_3N_4/\text{MIL-125-NH}_2$ heterojunction was synthesized, serving as the photocatalyst to generate ROS in POD. To determine the band structure of $g\text{-}C_3N_4/\text{MIL-125-NH}_2$, the method proposed by Kraut et al. was applied to calculate the band alignment between $g\text{-}C_3N_4$ and MIL-

125-NH₂ [71]. The core-level energy and upper edge of the valence band (VB) were obtained from XPS measurements (Fig. 4(a-c)). The bandgaps were determined from the UV–vis analysis (Fig. 4d). The valence band offset (VBO) was calculated with the following equation,

$$VBO = \left(E_{N-core}^{bulk} - E_{N-valence}^{bulk}\right) - \left(E_{Ti-core}^{bulk} - E_{Ti-valence}^{bulk}\right) - \left(E_{N-core}^{composite} - E_{Ti-core}^{composite}\right)$$
(3)

The conduction band offset (CBO) was determined by:

$$CBO = BG_{g-C_3N_4} + VBO - BG_{MIL-125-NH_2}$$
(4)

where E_{N-core}^{bulk} and $E_{Ti-core}^{bulk}$ are the core-level energies of bulk g-C₃N₄ and MIL-125-NH₂, respectively; $E_{N-valence}^{bulk}$ and $E_{Ti-valence}^{bulk}$ are the upper edges of VBs of g-C₃N₄ and MIL-125-NH₂, respectively. $E_{N-core}^{composite}$ – $E_{Ti-core}^{composite}$ indicates the core-level energy difference in the g-C₃N₄/MIL-125-NH₂ photocatalyst.

With the aforementioned information, an "S-scheme" heterojunction of g-C₃N₄/MIL-125-NH₂ with a precise alignment was mapped out (see Fig. 4e) [72-74]. In the heterojunction, MIL-125-NH₂ is the oxidation photocatalyst (OP) while g-C₃N₄ is the reduction photocatalyst (RP) [72]. When the two components come to contact, the electrons in g-C₃N₄ will drift to MIL-125-NH2 at the interface, hence g-C3N4 will lose electrons and become positively charged [72]. On the other hand, MIL-125-NH₂ will accept electrons and become negatively charged [72]. Naturally, an internal electric field is produced at the interface. When under light irradiation, the built-in electric field drives the photogenerated electrons from the conduction band (CB) of MIL-125-NH2 to the VB of g-C₃N₄. Meanwhile, the band edge of MIL-125-NH₂ bends upward due to the loss of electrons, but the band edge of g-C₃N₄ bends downward due to the accumulation of electrons [75]. The band bending and the Coulombic attraction between electrons in MIL-125-NH2 and holes in g-C₃N₄ favors photogenerated electrons charge transfer from the CB of MIL-125-NH2 to the VB of g-C3N4. Furthermore, the Coulombic repulsion, band bending, and built-in electric field can prevent the electron transfer from CB of g-C₃N₄ to CB of MIL-125-NH₂. Ultimately, the charge transfer is promoted and those photogenerated electrons and holes are reserved in the CB of g-C₃N₄ and VB of MIL-125-NH₂, respectively.

Therefore, this "S-scheme" heterojunction is expected to have better photocatalytic performance [72].

To determine the ROS species during photosynthesis, a ROSscavenger approach was used where various radical scavengers in the PBS solution along with g-C₃N₄/MIL-125-NH₂ [61]. Specifically, isopropyl alcohol (IPA, 0.2 mL), catalase (CAT, 10 mM), and p-benzoquinone (p-BO, 33.3 µM) were selected as the scavengers for •OH, H₂O₂, and $\bullet O_2$, respectively [61]. Considering the IPA and p-BQ are toxic to bacterial cells, which will result in errors in the analysis of results [76]. We replace the bacterial cells with a widely used model dye molecule, Rhodamine B [62]. As shown in SI 2, the photocatalytic degradation efficiency of Rhodamine B was achieved at 100 %, 100 %, and 9.7 % with the presence of IPA, CAT, and p-BQ, respectively. Apparently, the $\bullet O_2^-$ is the most dominant species in the photocatalytic system, as the addition of the $\bullet O_2^-$ scavengers (i.e., p-BQ) resulted in negligible photocatalytic degradation of Rhodamine B. Quantification of $\bullet O_2^-$ was carried out using the well-known 2,9-dimethyl-1,10-phenanthroline (DMP) method. Details on the calibration and measurement of $\bullet O_2^$ were listed in SI 2. The photocatalytic generated $\bullet O_2^-$ concentration for g- C_3N_4/MIL -125-NH $_2$ and QAC@g- C_3N_4/MIL -125-NH $_2$ were determined to be 20.64 µM and 18.34 µM, respectively. Both values are much larger than either g-C₃N₄ (2.16 µM) or MIL-125-NH₂ (14.14 µM), demonstrating the g-C₃N₄/MIL-125-NH₂ heterojunction did improve the photocatalysis. It should be noted that, after QAC coating, the BET surface area of QAC@g-C₃N₄/MIL-125-NH₂ (546.1 m²/g) is lower than that of g- $C_3N_4/MIL-125-NH_2$ (1040.1 m²/g) (see SI 5). The reduced specific surface area is caused by the grafted QAC polymer at the outer surface, which partially blocks the micropores of MIL-125-NH₂ (see Fig. S5(a, c)) [77]. Moreover, the peak of micropores from the MIL-125-NH₂ is significantly broadened and shifted to a more mesoporous structure in QAC@g-C₃N₄/MIL-125-NH₂ (see Fig. S5(b, d)). This is because, during the QAC coating process, g-C₃N₄/MIL-125-NH₂ was placed in a mixture of water and methanol solution containing several corrosive chemicals (e.g., CuBr and CuBr2), which may lead to partial degradation of MIL-125-NH₂ crystals by hydrolysis [78]. Since these micropores inside the materials are not fully involved in the photocatalytic reactions to provide active sites [79,80], a negligible difference was observed on $\bullet O_2$

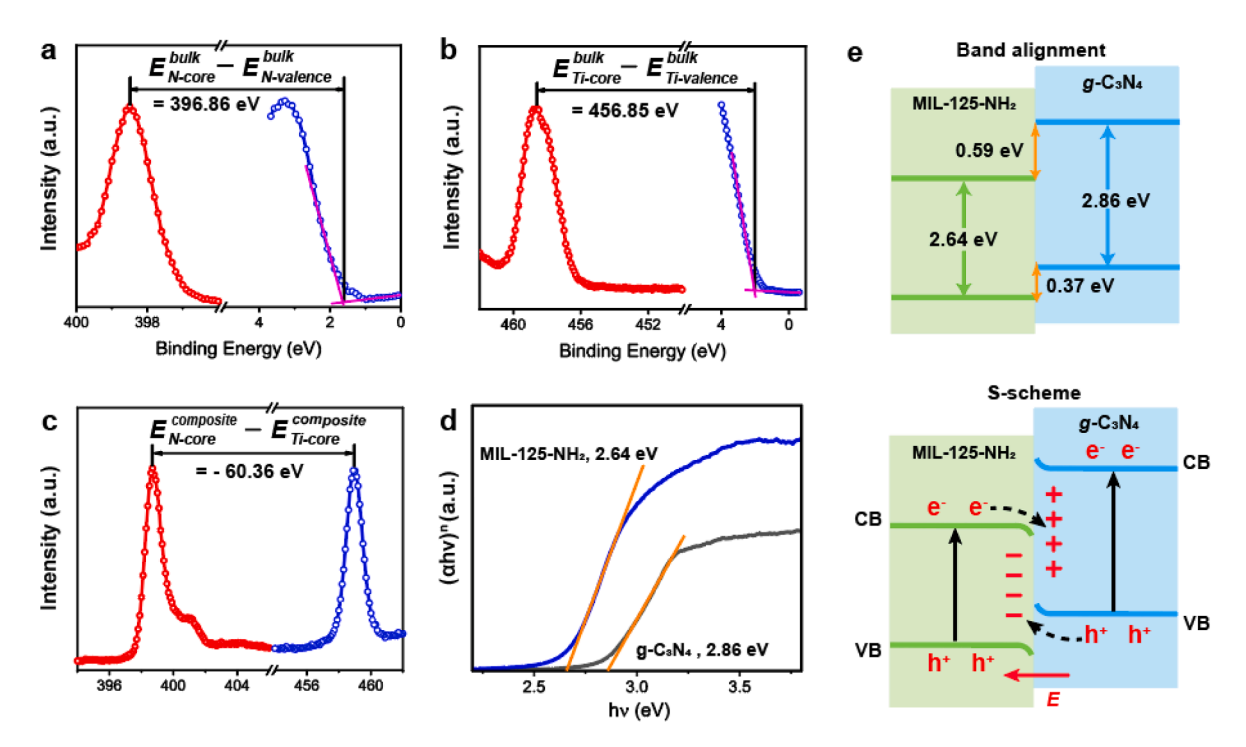


Fig. 4. XPS valence band and core-level spectra of (a) bulk g-C₃N₄, (b) bulk MIL-125-NH₂, and (c) g-C₃N₄/MIL-125-NH₂ composite; (d) Tauc plots of bulk g-C₃N₄ and MIL-125-NH₂; (e) schematic illustration of band alignment and charge transfer in g-C₃N₄/MIL-125-NH₂ heterojunction.

level between $g\text{-}C_3N_4/\text{MIL-}125\text{-}NH_2$ and QAC@ $g\text{-}C_3N_4/\text{MIL-}125\text{-}NH_2$, indicating that the $g\text{-}C_3N_4/\text{MIL-}125\text{-}NH_2$ heterostructure maintains its photocatalytic ROS generation even after the QAC modification.

3.4. Surface charges of QAC

Besides photocatalysis, the surface charges of the QAC coating were also examined. To elucidate the charge distribution of QAC on the photocatalyst, the near-surface elemental composition of g-C₃N₄/MIL-125-NH2 and QAC@g-C3N4/MIL-125-NH2 were firstly determined by XPS measurements in the dry state. Fig. 5(a, b) shows the deconvoluted N1s core level peaks of the samples. Both catalysts have three peaks at the same binding energies of 398.7 eV, 400.1 eV, and 401.2 eV, which are assigned to sp^2 -hybridized nitrogen (C-N=C), sp^3 -hybridized nitrogen in tertiary amine (N-(C)₃) and sp³-hybridized nitrogen in secondary amine (H-N-(C)₂), respectively [81]. The additional minor peak at 402.5 eV in OAC@g-C₃N₄/MIL-125-NH₂ corresponds to the quaternary nitrogen from QAC (NR₄⁺), once again indicative of the successful surface attachment of positively charged QAC on the surface [56]. By curve fitting of the high-resolution N 1 s XPS spectra, the relative area percentage of quaternary nitrogen NR₄⁺ is calculated to be 12.4 %. The relatively low percentage of quaternary nitrogen on the QAC@g-C3N4/ MIL-125-NH2 surface is probably caused by the g-C3N4 nanosheets wrapping around the composite, which leaves fewer QAC moieties to be counted within the detection limit of XPS (thickness: $0 \sim 10$ nm) [56].

In the POD system, photocatalysts and bacterial cells are in an aqueous solution. Thus it would be more realistic to investigate the surface charge of these particles by measuring their Zeta-potentials (ζ -potential) in liquid [82]. As shown in Fig. 5c, the variation in surface charge between g-C₃N₄/MIL-125-NH₂ and QAC@g-C₃N₄/MIL-125-NH₂ in PBS buffer (pH = 7.4) is more significant as compared to the dry state. g-C₃N₄/MIL-125-NH₂ has a negative ζ -potential of -22.7 mV while QAC@g-C₃N₄/MIL-125-NH₂ has a positive ζ -potential of 6.65 mV. It is because this layer of positively-charged QAC coating significantly alters

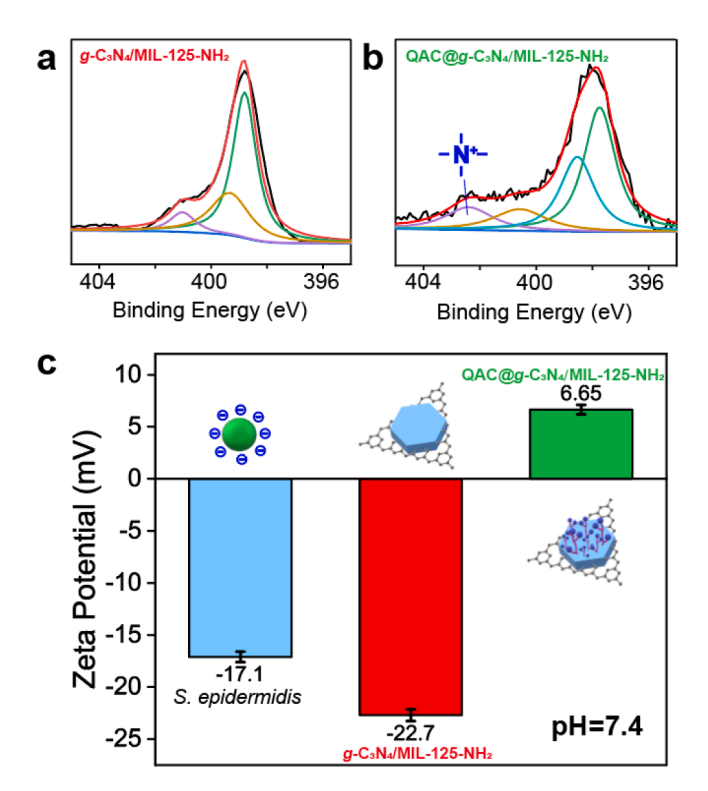


Fig. 5. XPS spectra of N 1 s of (a) g-C₃N₄/MIL-125-NH₂ and (b) QAC@g-C₃N₄/MIL-125-NH₂; (c) zeta potentials of *S. epidermidis*, g-C₃N₄/MIL-125-NH₂, and QAC@g-C₃N₄/MIL-125-NH₂ in PBS buffer (pH = 7.4).

the surface charging of the photocatalyst (i.e., $g\text{-}C_3N_4/\text{MIL-}125\text{-}NH_2$) from negative to positive. Moreover, S. epidermidis with a ζ -potential of -17.1 mV, like most bacterial cells in nature, are negatively charged due to the rich components of carboxylic and phosphate groups in the cell wall [45-47]. According to the well-known DLVO theory, which is used to quantitatively describes the force between charged interfaces in an aqueous solution, the electrostatic force (F_{el}) can be determined with the following simplified equation: [83,84].

$$F_{el} = \frac{4\pi R \sigma_1 \sigma_2 \lambda_D}{\varepsilon_e \varepsilon_0} e^{-\frac{d}{\lambda_D} \#}$$
 (5)

where R is the apex radius of material 1; σ_1 and σ_2 represent the surface charge density of material 1 and material 2, respectively; λ_D is the Debye length; ε_0 is the vacuum permittivity; ε_e is the dielectric permittivity of the electrolyte; and d is the distance between the two surfaces. Therefore, the opposite surface charges create a driving force for the electrostatic attraction between the QAC@g-C₃N₄/MIL-125-NH₂ (+6.65 mV) and bacterial cells (-17.1 mV) at the biointerface.

To visualize the interactions between the photocatalyst and bacterial cells caused by the charge modulation, a confocal laser scanning microscope (CLSM) was used. Specifically, bacterial cells were stained by the STYO/PI dye, which was visualized along with the materials under the CLSM observation. Fig. 6 shows S. epidermidis cells interact with g- $C_3N_4/MIL-125-NH_2$ (Fig. 6(a-c)) and OAC@g- $C_3N_4/MIL-125-NH_2$ (Fig. 6(d-f)) in dark for 1 h. For g-C₃N₄/MIL-125-NH₂ (-22.7 mV), the S. epidermidis cells are uniformly dispersed along with g-C₃N₄/MIL-125-NH2 particles in the PBS solution, but without significant affinity towards the g-C₃N₄/MIL-125-NH₂ surface (see Fig. 6a). This is due to the fact that both S. epidermidis cells and g-C₃N₄/MIL-125-NH₂ particles are negatively charged, which generates a repulsive electrostatic force to keep each other apart. After 1 h of interaction with g-C₃N₄/MIL-125-NH₂ in the dark, most S. epidermidis cells are alive and emit green fluorescence (Fig. 6b), which agrees with the bactericidal activities in Fig. 3. Moreover, the cell membranes of S. epidermidis are intact after g-C₃N₄/ MIL-125-NH₂ treatment as shown in Fig. 6c, indicating the bare g-C₃N₄/ MIL-125-NH2 causes little impact on the cell structures at the biointerface. For QAC@g-C₃N₄/MIL-125-NH₂ with a positive ζ-potential (+6.65 mV), a strong hetero-aggregation of S. epidermidis cells and QAC@g-C₃N₄/MIL-125-NH₂ particles was observed (see Fig. 6d). After 1 h, most S. epidermidis cells, especially for those located at the biointerface (insect in Fig. 6e), are dead and emit red fluorescence [55,56]. Exposed to the strong electrostatic force, the cell membranes are eventually destroyed and the cytoplasmatic is spread over the QAC@g-C3N4/ MIL-125-NH2 surface (see Fig. 6f). Therefore, this positively charged OAC layer can not only attract bacterial cells moving towards its surface but also destroy the cell membranes via the strong electrostatic force. Interestingly, for those bacterial cells far away from the biointerface, most of them are still alive and emit green fluorescence (see Fig. 6e), which is due to the relatively further distance between QAC@g-C3N4/ MIL-125-NH2 and bacterial cells dramatically decreasing the electrostatic interactions (see Eq. (5)).

All the above evidence suggests that the positively charged QAC layer significantly changed the bacterial movement at the biointerface. To further highlight the importance of bacteria-photocatalyst interaction in the POD activities under light irradiation, we broke down the POD experiment into "step-by-step" treatment: (i) photocatalytic ROS generation and (ii) QAC layer contact in the dark (see Fig. 7). Specifically, QAC@g-C₃N₄/MIL-125-NH₂ was the first subject to visible light irradiation to generate the ROS. Then, the bacterial cells were added to the above suspension, which was kept in the dark for 1 h. As shown in Fig. 7, the "step-by-step" treatment shows a significantly reduced bactericidal efficacy, compared to the "combined" POD treatment, and fewer colonies were found to grow in the agar plate. The less effective antibacterial property of "step-by-step" treatment is mainly caused by the following reasons. Under light irradiation, the photocatalytic

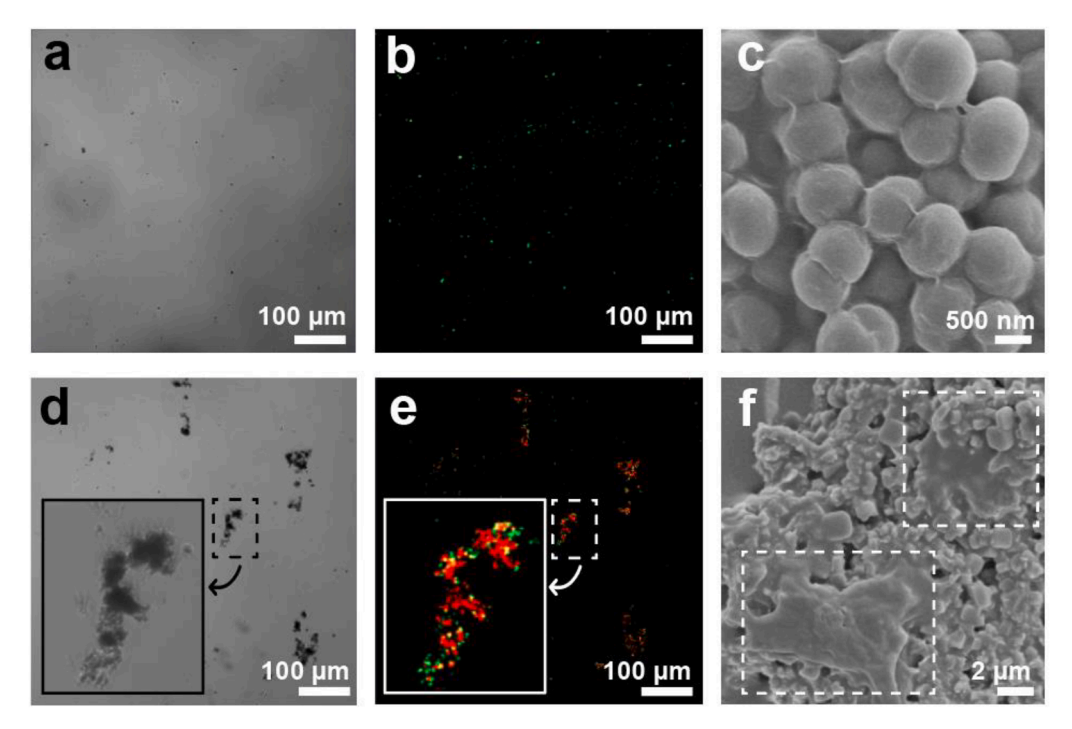


Fig. 6. Optical (a, d), confocal (b, e), and SEM (c, f) images of interactions at the biointerface. Panel (a-c): g-C₃N₄/MIL-125-NH₂ interacts with *S. epidermidis*; Panel (d-f): QAC@g-C₃N₄/MIL-125-NH₂ interacts with *S. epidermidis*.

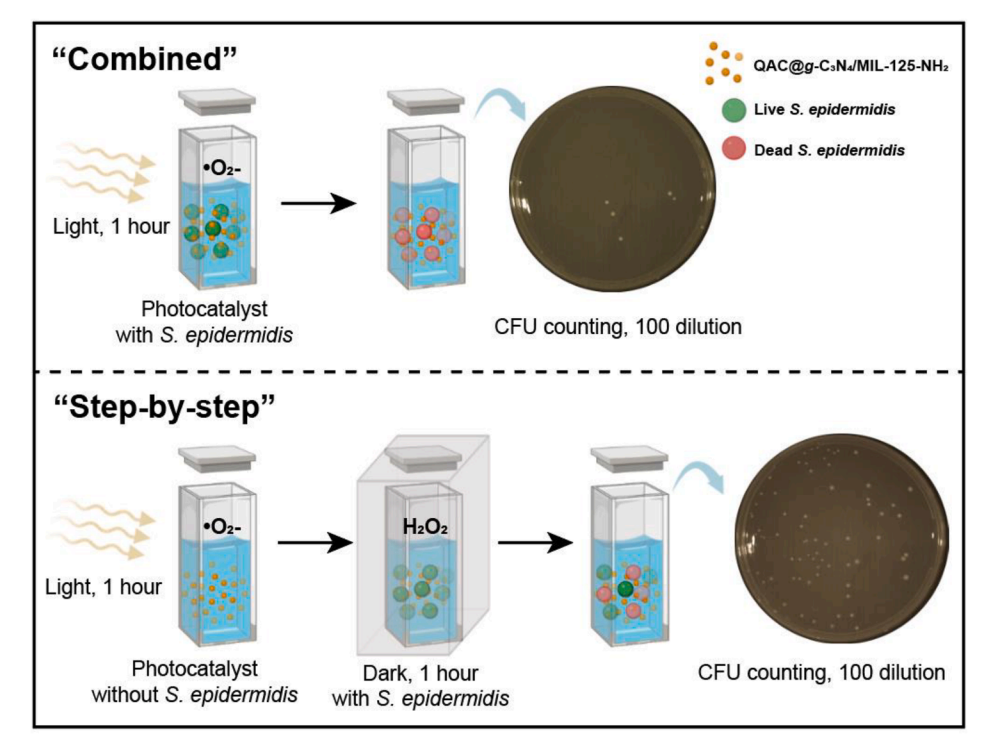


Fig. 7. Schematic diagram of two different approaches of photocatalytic oxidative disinfection of S. epidermidis.

generated $\cdot O_2^-$ (see SI 2) has a short half-life time of approximately 1 μs and can be easily degraded into less oxidative species such as H_2O_2 [27,85]. Due to these facts, the reactive $\cdot O_2^-$ that generated in the first cuvette during "step-by-step" treatment cannot be subsequently brought to the second cuvette containing QAC@g-C₃N₄/MIL-125-NH₂ (see Fig. 7). Therefore, an overall reduced bactericidal efficacy was observed in "step-by-step" treatment. Taken together, the mechanism of the positively charged QAC layer promotes photocatalyst-bacteria contact

and thus improves the overall POD performance can be concluded. In the "combined" treatment (see Fig. 7), the QAC layer helps attract the negatively charged bacterial cells moving towards the surface of the photocatalyst and shortens the distance between bacterial cells and the photocatalyst. When the light is further applied, the photogenerated short-lived $\cdot O_2^-$ can efficiently diffuse through the biointerface and be immediately used for disinfecting bacterial cells that attach on or near the QAC@g-C₃N₄/MIL-125-NH₂ surfaces. Therefore, a boosted POD

performance is achieved.

3.5. Visualization and quantification of bacteria-photocatalyst interactions

To further quantify the bacteria-photocatalyst interactions at the biointerface, the forces between the S. epidermidis cells and QAC@g-C₃N₄/MIL-125-NH₂ were investigated *via* the AFM force spectroscopy in PBS solution (pH 7.4), as illustrated in Fig. 8a. It should be noted that the measurement was carried out in the liquid rather than the air because the capillary forces that arise from the humid coverage of both the sample and the AFM tip under ambient conditions are significant, which will lead to errors in force data interpretation [83,86]. In a liquid environment, these capillary forces are absent [83,87]. For comparison, the pristine Si probe was functionalized with QAC@g-C3N4/MIL-125-NH₂ particles (Fig. 8 (b, c)) for the AFM measurement. Fig. 8d shows the peak force error image of the S. epidermidis cells using a pristine AFM Si probe as the control. The adhesion force mapping was also recorded with a resolution of 128×128 pixels (Fig. 8e). Under the PeakForce Quantitative Nano-Mechanics (QNM) mode, each pixel contains two force curves (i.e., approach and retrace). Sixteen randomly collected pixel data sets were averaged for the force-curve imaging. As shown in Fig. 8f, the separation in the X axis represents the distance of the AFM Si probe above the S. epidermidis surface. The force in Y-axis represents the interactive force between the AFM probe and S. epidermidis cells, where the positive sign indicates repulsion and vice versa. During the approach, the interactive force remains zero until the separation distance reaches

25 nm. At this point, the pre-set 2.0 nN force was applied between the pristine Si probe and S. epidermidis surface until the separation distance became zero. The distance of 25 nm is also regarded as the deformation of the S. epidermidis cells. After the Si probe tip snapped into the bacterial surface, the system starts to retrace the probe from the contact point to far away (separation = 300 nm). Typically, the value of the Y-axis at the lowest point in the retraction is defined as the adhesion force, which is considered the net effects of van der Waals force, acid-based interaction, and electrostatic interactions [49]. As shown in the blue line in Fig. 8f, a minor attractive adhesion force of 115 pN was observed in the trace process, which indicates the overall adhesion force is attractive. However, the adhesion force mapping of the S. epidermidis cell and force curve measured with QAC@g-C₃N₄/MIL-125-NH₂ modified Si probe are quite different (Fig. 8(g-i)). Due to a layer of positively charged QAC polymer on the surface, the attractive electrostatic effects in QAC@g-C₃N₄/MIL-125-NH₂ were observed much earlier than the bare Si probe in the approach curve, which starts at a much higher separation distance from 180 nm (Fig. 8i). Moreover, a significantly increased adhesion force of 972 pN was also detected in the QAC@g-C3N4/MIL-125-NH2 bacteria retrace curve, which indicates that, compared to the bare Si probe, the system has to provide larger force to separate the QAC@g-C₃N₄/MIL-125-NH₂ particle and *S. epidermidis* cells at the biointerface. The adhesion force data probed by the AFM between QAC@g-C3N4/MIL-125-NH₂ particles and S. epidermidis cells are in good agreement with the results observed in confocal images. By bridging the gaps between photocatalyst and bacterial cells at the biointerface, the photo-generated ROS on the photocatalyst can be fully used to kill the bacterial cells.

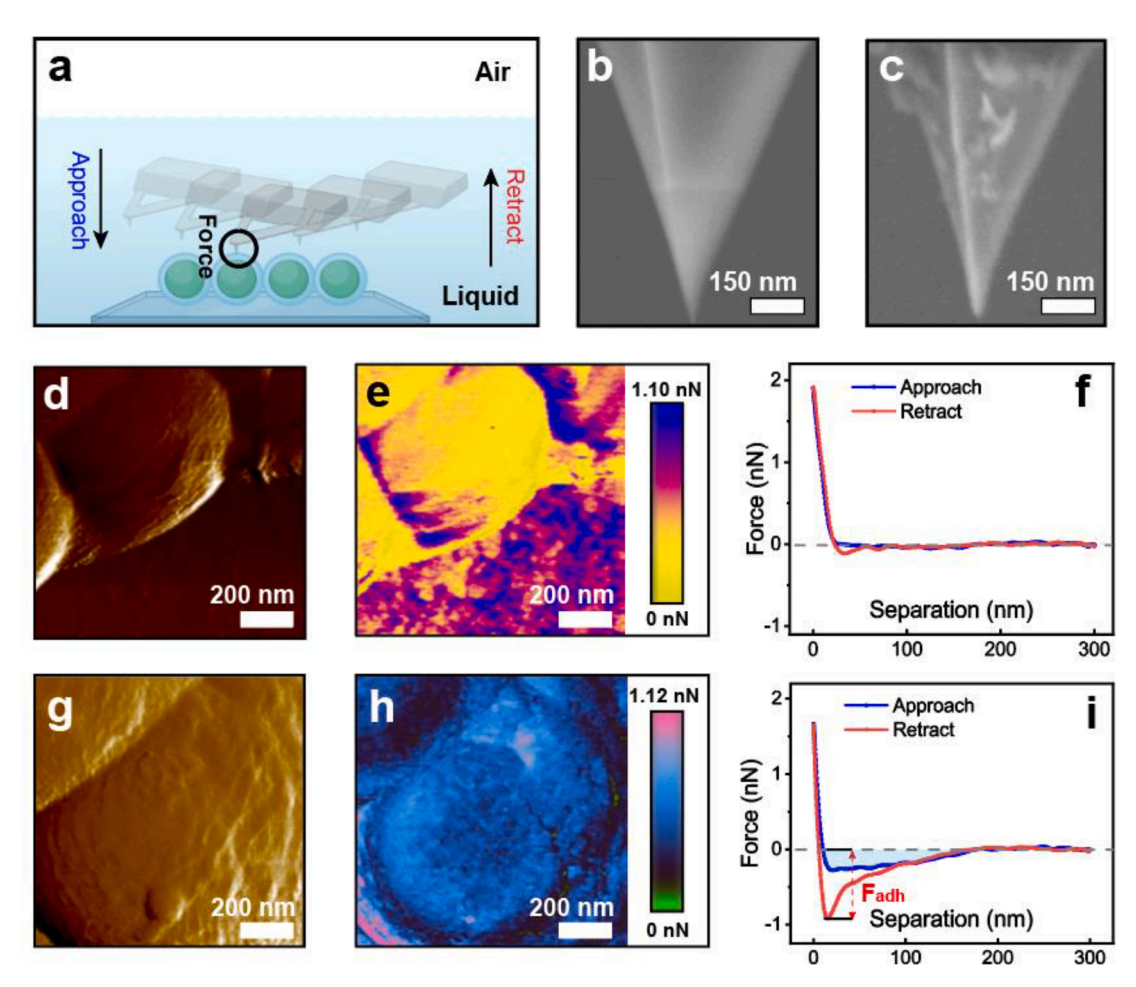


Fig. 8. AFM force measurements between *S. epidermidis* cells and the photocatalyst. (a) Illustration of the AFM force measurement in PBS solution; SEM images of (b) the pristine AFM Si probe and (c) the QAC@g-C₃N₄/MIL-125-NH₂ coated Si probe; (d,e,f) and (g,h,i) are the peak force error image, adhesion force mapping, and approach-retract force curves of *S. epidermidis* cells measured by using the pristine AFM probe and the photocatalyst-coated probe, respectively.

4. Conclusion

In summary, we have successfully developed a QAC@g-C_3N_4/MIL-125-NH_2 photocatalyst with a layer of positively charged QAC polymer-coated outside to improve the photocatalytic bactericidal activity. Experiments demonstrate that the QAC can positively modulate the surface charge and promote the bacteria-photocatalyst adhesion via electrostatic attraction, thus shortening the distance between photogenerated ROS and bacterial cells. Due to the effective usage of photogenerated ROS and bacteria-photocatalyst attraction at the biointerface, the photocatalytic disinfection performance is significantly improved. The assynthesized QAC@g-C_3N_4/MIL-125-NH_2 photocatalyst composite shows 3.20 logs of inactivation efficiency for Gram-positive (S. epidermidis) bacteria within 60 min under visible light irradiation. This study also provides a new avenue to strengthen the affinity between bacterial cells and photocatalyst at the biointerface via electrostatic attraction for POD applications.

Declaration of Competing Interest

The authors declare that they have no known competing financial interests or personal relationships that could have appeared to influence the work reported in this paper.

Data availability

Data will be made available on request.

Acknowledgments

This work was supported by the National Science Foundation, United States, award no. CMMI-1727553 to Dr. Wei-Ning Wang and the National Institutes of Health, award no. R01DE030121 to Dr. Ping Xu. We thank Prof. Sandro da Rocha and his group at Virginia Commonwealth University (VCU) for helping with the Zeta potential measurements. We thank Dr. Carl Mayer at Nanomaterials Characterization Center at VCU for his assistance in TEM characterization. We also acknowledge Prof. Mo Jiang and his group at VCU for the assistance in thermogravimetric analysis (TGA) data acquisition.

Appendix A. Supplementary data

Supplementary data to this article can be found online at https://doi.org/10.1016/j.cej.2022.139956.

References

- [1] S.F. Sia, L.M. Yan, A.W.H. Chin, K. Fung, K.T. Choy, A.Y.L. Wong, P. Kaewpreedee, R. Perera, L.L.M. Poon, J.M. Nicholls, M. Peiris, H.L. Yen, Pathogenesis and transmission of SARS-CoV-2 in golden hamsters, Nature 583 (7818) (2020) 834-+, https://doi.org/10.1038/s41586-020-2342-5.
- [2] S. Chang, E. Pierson, P.W. Koh, J. Gerardin, B. Redbird, D. Grusky, J. Leskovec, Mobility network models of COVID-19 explain inequities and inform reopening, Nature 589 (7840) (2021) 82–U54, https://doi.org/10.1038/s41586-020-2923-3.
- [3] E.J. Williamson, A.J. Walker, K. Bhaskaran, S. Bacon, C. Bates, C.E. Morton, H. J. Curtis, A. Mehrkar, D. Evans, P. Inglesby, J. Cockburn, H.I. McDonald, B. MacKenna, L. Tomlinson, I.J. Douglas, C.T. Rentsch, R. Mathur, A.Y.S. Wong, R. Grieve, D. Harrison, H. Forbes, A. Schultze, R. Croker, J. Parry, F. Hester, S. Harper, R. Perera, S.J.W. Evans, L. Smeeth, G. Ben, Factors associated with COVID-19-related death using OpenSAFELY, Nature 584 (7821) (2020) 430-+, https://doi.org/10.1038/s41586-020-2521-4.
- [4] C.JL. Murray, K.S. Ikuta, F. Sharara, L. Swetschinski, G. Robles Aguilar, A. Gray, C. Han, C. Bisignano, P. Rao, E. Wool, S.C. Johnson, A.J. Browne, M.G. Chipeta, F. Fell, S. Hackett, G. Haines-Woodhouse, B.H. Kashef Hamadani, E.A.P. Kumaran, B. McManigal, R. Agarwal, S. Akech, S. Albertson, J. Amuasi, J. Andrews, A. Aravkin, E. Ashley, F. Bailey, S. Baker, B. Basnyat, A. Bekker, R. Bender, A. Bethou, J. Bielicki, S. Boonkasidecha, J. Bukosia, C. Carvalheiro, C. Castañeda-Orjuela, V. Chansamouth, S. Chaurasia, S. Chiurchiù, F. Chowdhury, A.J. Cook, B. Cooper, T.R. Cressey, E. Criollo-Mora, M. Cunningham, S. Darboe, N.P.J. Day, M. De Luca, K. Dokova, A. Dramowski, S.J. Dunachie, T. Eckmanns, D. Eibach, A. Emami, N. Feasey, N. Fisher-Pearson, K. Forrest, D. Garrett, P. Gastmeier, A. Z. Giref, R.C. Greer, V. Gupta, S. Haller, A. Haselbeck, S.I. Hay, M. Holm,

- S. Hopkins, K.C. Iregbu, J. Jacobs, D. Jarovsky, F. Javanmardi, M. Khorana, N. Kissoon, E. Kobeissi, T. Kostyanev, F. Krapp, R. Krumkamp, A. Kumar, H.H. Kyu, C. Lim, D. Limmathurotsakul, M.J. Loftus, M. Lunn, J. Ma, N. Mturi, T. Munera-Huertas, P. Musicha, M.M. Mussi-Pinhata, T. Nakamura, R. Nanavati, S. Nangia, P. Newton, C. Ngoun, A. Novotney, D. Nwakanma, C.W. Obiero, A. Olivas-Martinez, P. Olliaro, E. Ooko, E. Ortiz-Brizuela, A.Y. Peleg, C. Perrone, N. Plakkal, A. Ponce-de-Leon, M. Raad, T. Ramdin, A. Riddell, T. Roberts, J.V. Robotham, A. Roca, K.E. Rudd, N. Russell, J. Schnall, J.A.G. Scott, M. Shivamallappa, J. Sifuentes-Osornio, N. Steenkeste, A.J. Stewardson, T. Stoeva, N. Tasak, A. Thaiprakong, G. Thwaites, C. Turner, P. Turner, H.R. van Doorn, S. Velaphi, A. Vongpradith, H. Vu, T. Walsh, S. Waner, T. Wangrangsimakul, T. Wozniak, P. Zheng, B. Sartorius, A.D. Lopez, A. Stergachis, C. Moore, C. Dolecek, M. Naghavi, Global burden of bacterial antimicrobial resistance in 2019: a systematic analysis, The Lancet 399 (10325) (2022) 629–655.
- [5] D.J. Anderson, L.F. Chen, D.J. Weber, R.W. Moehring, S.S. Lewis, P.F. Triplett, M. Blocker, P. Becherer, J.C. Schwab, L.P. Knelson, Y. Lokhnygina, W.A. Rutala, H. Kanamori, M.F. Gergen, D.J. Sexton, Enhanced terminal room disinfection and acquisition and infection caused by multidrug-resistant organisms and Clostridium difficile (the Benefits of Enhanced Terminal Room Disinfection study): a cluster-randomised, multicentre, crossover study, The Lancet 389 (10071) (2017) 805–814. https://doi.org/10.1016/S0140-6736(16)31588-4.
- [6] S.S. Magill, J.R. Edwards, W. Bamberg, Z.G. Beldavs, G. Dumyati, M.A. Kainer, R. Lynfield, M. Maloney, L. McAllister-Hollod, J. Nadle, S.M. Ray, D.L. Thompson, L.E. Wilson, S.K. Fridkin, Multistate Point-Prevalence Survey of Health Care-Associated Infections, New Engl. J. Med. 370 (13) (2014) 1198–1208, https://doi. org/10.1056/NEJMoa1306801.
- [7] J.W. Leavitt, Typhoid Mary: captive to the public's health, Beacon Press, 1997.
- [8] A.K. Pitol, T.R. Julian, Community transmission of SARS-CoV-2 by surfaces: risks and risk reduction strategies, Environ. Sci. Technol. Lett. 8 (3) (2021) 263–269, https://doi.org/10.1021/acs.estlett.0c00966.
- [9] P.L. Remington, W.N. Hall, I.H. Davis, A. Herald, R.A. Gunn, Airborne transmission of measles in a physician's office, JAMA 253 (11) (1985) 1574–1577, https://doi. org/10.1001/jama.1985.03350350068022.
- [10] H. Kitagawa, T. Nomura, T. Nazmul, K. Omori, N. Shigemoto, T. Sakaguchi, H. Ohge, Effectiveness of 222-nm ultraviolet light on disinfecting SARS-CoV-2 surface contamination, Am. J. Infect. Control 49 (3) (2021) 299–301, https://doi. org/10.1016/j.aiic.2020.08.022.
- [11] Y.e. Yang, X. Wu, L. Ma, C. He, S. Cao, Y. Long, J. Huang, R.D. Rodriguez, C. Cheng, C. Zhao, L.i. Qiu, Bioinspired spiky peroxidase-mimics for localized bacterial capture and synergistic catalytic sterilization, Adv. Mater. 33 (8) (2021) 2005477.
- [12] L. Liao, W. Xiao, M.V. Zhao, X.Z. Yu, H.T. Wang, Q.Q. Wang, S. Chu, Y. Cui, Can N95 respirators be reused after disinfection? how many times? ACS Nano 14 (5) (2020) 6348–6356, https://doi.org/10.1021/acsnano.0c03597.
- [13] C. Weiss, M. Carriere, L. Fusco, I. Capua, J.A. Regla-Nava, M. Pasquali, A.A. Scott, F. Vitale, M.A. Unal, C. Mattevi, D. Bedognetti, A. Merkoci, E. Tasciotti, A. Yilmazer, Y. Gogotsi, F. Stellacci, L.G. Delogu, Toward nanotechnology-enabled approaches against the COVID-19 pandemic, ACS Nano 14 (6) (2020) 6383–6406, https://doi.org/10.1021/acsnano.0c03697.
- [14] Z.Y. Teng, N.L. Yang, H.Y. Lv, S.C. Wang, M.Z. Hu, C.Y. Wang, D. Wang, G. X. Wang, Edge-functionalized g-C3N4 nanosheets as a highly efficient metal-free photocatalyst for safe drinking water, CHEM 5 (3) (2019) 664–680, https://doi.org/10.1016/j.chempr.2018.12.009.
- [15] W.J. Wang, J.C. Yu, D.H. Xia, P.K. Wong, Y.C. Li, Graphene and g-C3N4 nanosheets cowrapped elemental alpha-sulfur as a novel metal-free heterojunction photocatalyst for bacterial inactivation under visible-light, Environ. Sci. Technol. 47 (15) (2013) 8724–8732, https://doi.org/10.1021/es4013504.
- [16] Y. Kim, E. Coy, H. Kim, R. Mrówczyński, P. Torruella, D.-W. Jeong, K.S. Choi, J. H. Jang, M.Y. Song, D.-J. Jang, F. Peiro, S. Jurga, H.J. Kim, Efficient photocatalytic production of hydrogen by exploiting the polydopamine-semiconductor interface, Appl. Catal. B Environ. 280 (2021) 119423.
- [17] H. Shi, J. Fan, Y. Zhao, X. Hu, X.u. Zhang, Z. Tang, Visible light driven CuBi2O4/ Bi2MoO6 p-n heterojunction with enhanced photocatalytic inactivation of E. coli and mechanism insight, J. Hazard. Mater. 381 (2020) 121006.
- [18] P. Li, J. Li, X. Feng, J. Li, Y. Hao, J. Zhang, H. Wang, A. Yin, J. Zhou, X. Ma, B. Wang, Metal-organic frameworks with photocatalytic bactericidal activity for integrated air cleaning, Nat. Commun. 10 (1) (2019) 2177, https://doi.org/ 10.1038/s41467-019-10218-9.
- [19] A. Kumar, P. Raizada, P. Singh, R.V. Saini, A.K. Saini, A. Hosseini-Bandegharaei, Perspective and status of polymeric graphitic carbon nitride based Z-scheme photocatalytic systems for sustainable photocatalytic water purification, Chem. Eng. J. 391 (2020) 123496.
- [20] W. Wang, C. Zhou, Y. Yang, G. Zeng, C. Zhang, Y. Zhou, J. Yang, D. Huang, H. Wang, W. Xiong, X. Li, Y. Fu, Z. Wang, Q. He, M. Jia, H. Luo, Carbon nitride based photocatalysts for solar photocatalytic disinfection, can we go further? Chem. Eng. J. 404 (2021) 126540.
- [21] Y. Orooji, M. Ghanbari, O. Amiri, M. Salavati-Niasari, Facile fabrication of silver iodide/graphitic carbon nitride nanocomposites by notable photo-catalytic performance through sunlight and antimicrobial activity, J. Hazard. Mater. 389 (2020), 122079, https://doi.org/10.1016/j.jhazmat.2020.122079.
- [22] S. Horikoshi, N. Serpone, Can the photocatalyst TiO2 be incorporated into a wastewater treatment method? Background and prospects, Catal. Today 340 (2020) 334–346, https://doi.org/10.1016/j.cattod.2018.10.020.
- [23] C. Zhang, Y. Li, D.M. Shuai, Y. Shen, W. Xiong, L.Q. Wang, Graphitic carbon nitride (g-C3N4)-based photocatalysts for water disinfection and microbial control: A review, Chemosphere 214 (2019) 462–479, https://doi.org/10.1016/j. chemosphere.2018.09.137.

- [24] J.H. You, Y.Z. Guo, R. Guo, X.W. Liu, A review of visible light-active photocatalysts for water disinfection: Features and prospects, Chem. Eng. J. 373 (2019) 624–641, https://doi.org/10.1016/j.cej.2019.05.071.
- [25] X.K. Zeng, Z.Y. Wang, G. Wang, T.R. Gengenbach, D.T. McCarthy, A. Deletic, J. G. Yu, X.W. Zhang, Highly dispersed TiO2 nanocrystals and WO3 nanorods on reduced graphene oxide: Z-scheme photocatalysis system for accelerated photocatalytic water disinfection, Appl. Catal. B Environ. 218 (2017) 163–173, https://doi.org/10.1016/j.apcatb.2017.06.055.
- [26] J. Song, H. Kong, J. Jang, Bacterial adhesion inhibition of the quaternary ammonium functionalized silica nanoparticles, Colloids Surf. B Biointerfaces 82 (2) (2011) 651–656. https://doi.org/10.1016/j.colsurfb.2010.10.027.
- [27] P. Sharma, A.B. Jha, R.S. Dubey, M. Pessarakli, Reactive Oxygen Species, Oxidative Damage, and Antioxidative Defense Mechanism in Plants under Stressful Conditions, J. Botany 2012 (2012), 217037.
- [28] D. Xu, D. Liu, B. Wang, C. Chen, Z. Chen, D. Li, Y. Yang, H. Chen, M.G. Kong, M. Yousfi, In Situ OH Generation from O2— and H2O2 Plays a Critical Role in Plasma-Induced Cell Death, PLoS ONE 10 (6) (2015) e0128205, https://doi.org/10.1371/journal.pone.0128205.
- [29] Y. Nosaka, A.Y. Nosaka, Generation and Detection of Reactive Oxygen Species in Photocatalysis, Chem. Rev. 117 (17) (2017) 11302–11336, https://doi.org/ 10.1021/acs.chemrev.7b00161.
- [30] J.V.L. Nguyen, E. Ghafar-Zadeh, Biointerface materials for cellular adhesion: recent progress and future prospects, Actuators 9 (4) (2020), https://doi.org/10.3390/ act9040137.
- [31] A.M. Nasir, N. Awang, S.K. Hubadillah, J. Jaafar, M.H.D. Othman, W.N. Wan Salleh, A.F. Ismail, A review on the potential of photocatalysis in combatting SARS-CoV-2 in wastewater, Journal of Water, Process Eng. 42 (2021), https://doi.org/ 10.1016/j.jwpe.2021.102111.
- [32] X. He, W.-N. Wang, MOF-based ternary nanocomposites for better CO2 photoreduction: roles of heterojunctions and coordinatively unsaturated metal sites, J. Mater. Chem. A 6 (3) (2018) 932–940, https://doi.org/10.1039/c7ta09192c
- [33] H. Wang, X. Yuan, Y. Wu, G. Zeng, X. Chen, L. Leng, H. Li, Synthesis and applications of novel graphitic carbon nitride/metal-organic frameworks mesoporous photocatalyst for dyes removal, Appl. Catal. B Environ. 174–175 (2015) 445–454. https://doi.org/10.1016/j.apeatb.2015.03.037.
- [34] W.J. Ong, L.L. Tan, Y.H. Ng, S.T. Yong, S.P. Chai, Graphitic Carbon Nitride (g-C3N4)-Based Photocatalysts for Artificial Photosynthesis and Environmental Remediation: Are We a Step Closer To Achieving Sustainability? Chem. Rev. 116 (12) (2016) 7159–7329, https://doi.org/10.1021/acs.chemrev.6b00075.
- [35] C. Li, Z. Sun, W. Zhang, C. Yu, S. Zheng, Highly efficient g-C3N4/TiO2/kaolinite composite with novel three-dimensional structure and enhanced visible light responding ability towards ciprofloxacin and S. aureus, Appl. Catal. B 220 (2018) 272–282.
- [36] N. Lu, M. Zhang, X. Jing, P. Zhang, Y. Zhu, Z. Zhang, Electrospun Semiconductor-Based Nano-Heterostructures for Photocatalytic Energy Conversion and Environmental Remediation: Opportunities and Challenges, ENERGY & ENVIRONMENTAL MATERIALS n/a(n/a) (2021). https://doi.org/https://doi.org/10.1002/eem2.12338.
- [37] W. Lu, T. Ding, N. Lu, J. Zhang, K. Yun, P. Zhang, Z. Zhang, Engineering continuous charge steps in multiple 2D-semiconductor hetero-interface for rapidly photocatalytic dye-degradation and disinfection, Appl. Surf. Sci. 592 (2022), 153348. https://doi.org/10.1016/j.apsusc.2022.153348.
- [38] S. Romero-Vargas Castrillón, F. Perreault, A.F. de Faria, M. Elimelech, Interaction of Graphene Oxide with Bacterial Cell Membranes: Insights from Force Spectroscopy, Environ. Sci. Technol. Lett. 2 (4) (2015) 112–117, https://doi.org/ 10.1021/acs.estlett.5b00066.
- [39] X. Zeng, Y. Liu, Y. Xia, M.H. Uddin, D. Xia, D.T. McCarthy, A. Deletic, J. Yu, X. Zhang, Cooperatively modulating reactive oxygen species generation and bacteria-photocatalyst contact over graphitic carbon nitride by polyethylenimine for rapid water disinfection, Appl. Catal. B Environ. 274 (2020), 119095. https://doi.org/10.1016/j.apcatb.2020.119095.
- [40] X. Zeng, Y. Liu, Y. Kang, Q. Li, Y. Xia, Y. Zhu, H. Hou, M.H. Uddin, T. R. Gengenbach, D. Xia, C. Sun, D.T. McCarthy, A. Deletic, J. Yu, X. Zhang, Simultaneously Tuning Charge Separation and Oxygen Reduction Pathway on Graphitic Carbon Nitride by Polyethylenimine for Boosted Photocatalytic Hydrogen Peroxide Production, ACS Catal. 10 (6) (2020) 3697–3706, https://doi.org/10.1021/acscatal.9b05247.
- [41] E. Kusiak-Nejman, A.W. Morawski, TiO2/graphene-based nanocomposites for water treatment: A brief overview of charge carrier transfer, antimicrobial and photocatalytic performance, Appl. Catal. B 253 (2019) 179–186. https://doi.org/10.1016/j.apcatb.2019.04.055.
- [42] K. Das, A. Roychoudhury, Reactive oxygen species (ROS) and response of antioxidants as ROS-scavengers during environmental stress in plants, Front. Environ. Sci. 2 (2014).
- [43] S. Hippeli, E.F. Elstner, OH-Radical-Type Reactive Oxygen Species: A Short Review on the Mechanisms of OH-Radical-and Peroxynitrite Toxicity, Zeitschrift für Naturforschung C 52(9-10) (1997) 555-563. https://doi.org/doi:10.1515/znc-1997-9-1001.
- [44] Y.F. Dufrêne, A. Persat, Mechanomicrobiology: how bacteria sense and respond to forces, Nat. Rev. Microbiol. 18 (4) (2020) 227–240, https://doi.org/10.1038/ s41579-019-0314-2.
- [45] Z. Zhu, Y.u. Zhang, L. Bao, J. Chen, S. Duan, S.-C. Chen, P. Xu, W.-N. Wang, Self-decontaminating nanofibrous filters for efficient particulate matter removal and airborne bacteria inactivation, Environ. Sci. Nano 8 (4) (2021) 1081–1095.

- [46] Y. Zhang, X. Zhang, Y.-Q. Zhao, X.-Y. Zhang, X. Ding, X. Ding, B. Yu, S. Duan, F.-J. Xu, Self-adaptive antibacterial surfaces with bacterium-triggered antifoulingbactericidal switching properties, Biomater. Sci. 8 (3) (2020) 997–1006, https:// doi.org/10.1039/C9BM01666J.
- [47] S. Venkata Mohan, P. Chiranjeevi, K. Chandrasekhar, P.S. Babu, O. Sarkar, Chapter 11 Acidogenic Biohydrogen Production From Wastewater, in: A. Pandey, S.V. Mohan, J.-S. Chang, P.C. Hallenbeck, C. Larroche (Eds.), Biohydrogen (Second Edition), Elsevier2019, pp. 279-320. https://doi.org/https://doi.org/10.1016/B978-0-444-64203-5.00011-3.
- [48] M. Cho, H. Chung, W. Choi, J. Yoon, Linear correlation between inactivation of E. coli and OH radical concentration in TiO2 photocatalytic disinfection, Water Res. 38 (4) (2004) 1069–1077. https://doi.org/10.1016/j.watres.2003.10.029.
- [49] S. Bayoudh, A. Othmane, L. Mora, H. Ben Ouada, Assessing bacterial adhesion using DLVO and XDLVO theories and the jet impingement technique, Colloids Surf B. Biointerfaces 73 (1) (2009) 1–9. https://doi.org/10.1016/j.colsurfb.2009.04.0
- [50] A.E. Nel, L. Mädler, D. Velegol, T. Xia, E.M.V. Hoek, P. Somasundaran, F. Klaessig, V. Castranova, M. Thompson, Understanding biophysicochemical interactions at the nano-bio interface, Nat. Mater. 8 (7) (2009) 543–557, https://doi.org/ 10.1038/nmat2442.
- [51] C.J. van Oss, Acid—base interfacial interactions in aqueous media, Colloids Surf. A 78 (1993) 1–49. https://doi.org/10.1016/0927-7757(93)80308-2.
- [52] A.P. Demchenko, Introduction to fluorescence sensing, 2nd ed., Springer, Switzerland, 2015.
- [53] J. Zhou, Z. Hu, F. Zabihi, Z. Chen, M. Zhu, Progress and perspective of antiviral protective material, Adv. Fiber Mater. 2 (3) (2020) 123–139, https://doi.org/ 10.1007/s42765-020-00047-7.
- [54] A. Habibi-Yangjeh, S. Asadzadeh-Khaneghah, S. Feizpoor, A. Rouhi, Review on heterogeneous photocatalytic disinfection of waterborne, airborne, and foodborne viruses: Can we win against pathogenic viruses? J. Colloid Interfaces Sci. 580 (2020) 503–514. https://doi.org/10.1016/j.jcis.2020.07.047.
- [55] Y. Jiao, L.-N. Niu, S. Ma, J. Li, F.R. Tay, J.-H. Chen, Quaternary ammonium-based biomedical materials: State-of-the-art, toxicological aspects and antimicrobial resistance, Prog. Polym. Sci. 71 (2017) 53–90, https://doi.org/10.1016/j. progpolymsci.2017.03.001.
- [56] K. Chen, S.P. Nikam, Z.K. Zander, Y.-H. Hsu, N.Z. Dreger, M. Cakmak, M.L. Becker, Continuous fabrication of antimicrobial nanofiber mats using post-electrospinning functionalization for roll-to-roll scale-up, ACS Appl. Polym. Mater. 2 (2) (2020) 304–316, https://doi.org/10.1021/acsapm.9b00798.
- [57] Z. Zhu, X. He, W.-N. Wang, Unraveling the origin of the "Turn-On" effect of Al-MIL-53-NO2 during H2S detection, CrystEngComm 22 (2) (2020) 195–204, https://doi.org/10.1039/C9CE01595G.
- [58] Q. Xiang, J. Yu, M. Jaroniec, Preparation and enhanced visible-light photocatalytic H2-production activity of graphene/C3N4 composites, J. Phys. Chem. C 115 (15) (2011) 7355–7363, https://doi.org/10.1021/jp200953k.
- [59] D. Wang, S.E. Gilliland, X. Yi, K. Logan, D.R. Heitger, H.R. Lucas, W.-N. Wang, Iron mesh-based metal organic framework filter for efficient arsenic removal, Environ. Sci. Technol. 52 (7) (2018) 4275–4284, https://doi.org/10.1021/acs.est.7b06212.
- [60] X. He, V. Nguyen, Z. Jiang, D. Wang, Z. Zhu, W.-N. Wang, Highly-oriented onedimensional MOF-semiconductor nanoarrays for efficient photodegradation of antibiotics, Catal. Sci. Technol. 8 (8) (2018) 2117–2123, https://doi.org/10.1039/ c8cy00229k.
- [61] K.J. Heo, S.B. Jeong, J. Shin, G.B. Hwang, H.S. Ko, Y. Kim, D.Y. Choi, J.H. Jung, Water-Repellent TiO2-Organic Dye-Based Air Filters for Efficient Visible-Light-Activated Photochemical Inactivation against Bioaerosols, Nano Lett. 21 (4) (2021) 1576–1583. https://doi.org/10.1021/acs.panolett.0r03173.
- 1576–1583, https://doi.org/10.1021/acs.nanolett.0c03173.
 [62] S.C. Yan, Z.S. Li, Z.G. Zou, Photodegradation of Rhodamine B and Methyl Orange over Boron-Doped g-C3N4 under Visible Light Irradiation, Langmuir 26 (6) (2010) 3894–3901, https://doi.org/10.1021/la904023j.
- [63] D. Wang, B. Zhu, X. He, Z. Zhu, G. Hutchins, P. Xu, W.-N. Wang, Iron oxide nanowire-based filter for inactivation of airborne bacteria, Environ. Sci. Nano 5 (5) (2018) 1096–1106, https://doi.org/10.1039/c8en00133b.
- [64] N. Gavara, A beginner's guide to atomic force microscopy probing for cell mechanics, Microsc. Res. Tech. 80 (1) (2017) 75–84, https://doi.org/10.1002/ jent 22776
- [65] E. Koufakis, T. Manouras, S.H. Anastasiadis, M. Vamvakaki, Film Properties and Antimicrobial Efficacy of Quaternized PDMAEMA Brushes: Short vs Long Alkyl Chain Length, Langmuir 36 (13) (2020) 3482–3493, https://doi.org/10.1021/acs. langmuir 0b03266
- [66] Y. Zhao, W. Cai, J. Chen, Y. Miao, Y. Bu, A Highly Efficient Composite Catalyst Constructed From NH2-MIL-125(Ti) and Reduced Graphene Oxide for CO2 Photoreduction, Front. Chem. 7 (2019) 789.
- [67] E.M. Pérez, N. Martín, π-π interactions in carbon nanostructures, Chem. Soc. Rev. 44 (18) (2015) 6425–6433, https://doi.org/10.1039/C5CS00578G.
 [68] L. Liu, D. Zhang, Y. Zhu, Y. Han, Bulk and local structures of metal-organic
- [68] L. Liu, D. Zhang, Y. Zhu, Y. Han, Bulk and local structures of metal-organic frameworks unravelled by high-resolution electron microscopy, Commun. Chem. 3 (1) (2020) 99, https://doi.org/10.1038/s42004-020-00361-6.
- [69] Y. Chen, T.W. Ng, A. Lu, Y. Li, H.Y. Yip, T. An, G. Li, H. Zhao, M. Gao, P.K. Wong, Comparative study of visible-light-driven photocatalytic inactivation of two different wastewater bacteria by natural sphalerite, Chem. Eng. J. 234 (2013) 43–48. https://doi.org/10.1016/j.cej.2013.08.106.
- [70] R. Kaur, S. Liu, Antibacterial surface design Contact kill, Prog. Surf. Sci. 91 (3) (2016) 136–153. https://doi.org/10.1016/j.progsurf.2016.09.001.
- [71] E.A. Kraut, R.W. Grant, J.R. Waldrop, S.P. Kowalczyk, Precise Determination of the Valence-Band Edge in X-Ray Photoemission Spectra: Application to Measurement

- of Semiconductor Interface Potentials, Phys. Rev. Lett. 44 (24) (1980) 1620–1623, https://doi.org/10.1103/PhysRevLett.44.1620.
- [72] L. Zhang, J. Zhang, H. Yu, J. Yu, Emerging S-Scheme Photocatalyst, Adv. Mater. 34 (11) (2022) 2107668. https://doi.org/10.1002/adma.202107668.
- [73] Q. Xu, S. Wageh, A.A. Al-Ghamdi, X. Li, Design principle of S-scheme heterojunction photocatalyst, J. Mater. Sci. Technol. 124 (2022) 171–173. htt ps://doi.org/10.1016/j.jimst.2022.02.016.
- [74] X. Li, B. Kang, F. Dong, Z. Zhang, X. Luo, L. Han, J. Huang, Z. Feng, Z. Chen, J. Xu, B. Peng, Z.L. Wang, Enhanced photocatalytic degradation and H2/H2O2 production performance of S-pCN/WO2.72 S-scheme heterojunction with appropriate surface oxygen vacancies, Nano Energy 81 (2021), 105671. https://doi.org/10.1016/j.nanoen.2020.105671.
- [75] J. Fu, Q. Xu, J. Low, C. Jiang, J. Yu, Ultrathin 2D/2D WO3/g-C3N4 step-scheme H2-production photocatalyst, Appl. Catal. B 243 (2019) 556–565. https://doi.org/10.1016/j.apcatb.2018.11.011.
- [76] E.N. Carcamo-Noriega, S. Sathyamoorthi, S. Banerjee, E. Gnanamani, M. Mendoza-Trujillo, D. Mata-Espinosa, R. Hernández-Pando, J.I. Veytia-Bucheli, L.D. Possani, R.N. Zare, 1,4-Benzoquinone antimicrobial agents against Staphylococcus aureus and Mycobacterium tuberculosis derived from scorpion venom, PNAS 116 (26) (2019) 12642–12647.
- [77] H. Molavi, A. Shojaei, S.A. Mousavi, Improving mixed-matrix membrane performance via PMMA grafting from functionalized NH2–UiO-66, J. Mater. Chem. A 6 (6) (2018) 2775–2791, https://doi.org/10.1039/C7TA10480D.
- [78] A. Gómez-Avilés, V. Muelas-Ramos, J. Bedia, J.J. Rodriguez, C. Belver, Thermal Post-Treatments to Enhance the Water Stability of NH2-MIL-125(Ti), Catalysts, 2020
- [79] Y. Ma, X. Yi, S. Wang, T. Li, B. Tan, C. Chen, T. Majima, E.R. Waclawik, H. Zhu, J. Wang, Selective photocatalytic CO2 reduction in aerobic environment by microporous Pd-porphyrin-based polymers coated hollow TiO2, Nat. Commun. 13 (1) (2022) 1400, https://doi.org/10.1038/s41467-022-29102-0.
- [80] D. Jiang, P. Xu, H. Wang, G. Zeng, D. Huang, M. Chen, C. Lai, C. Zhang, J. Wan, W. Xue, Strategies to improve metal organic frameworks photocatalyst's

- performance for degradation of organic pollutants, Coord. Chem. Rev. 376 (2018) 449–466. https://doi.org/10.1016/j.ccr.2018.08.005.
- [81] Y. Sun, C. Li, Y. Xu, H. Bai, Z. Yao, G. Shi, Chemically converted graphene as substrate for immobilizing and enhancing the activity of a polymeric catalyst, Chem. Commun. 46 (26) (2010) 4740–4742, https://doi.org/10.1039/C001635G.
- [82] K. Pate, P. Safier, 12 Chemical metrology methods for CMP quality, in: S. Babu (Ed.), Advances in Chemical Mechanical Planarization (CMP), Woodhead Publishing, 2016, pp. 299–325.
- [83] M.W. Amrein, D. Stamov, in: Atomic Force Microscopy in the Life Sciences, Springer Handbook of Microscopy, Springer International Publishing, Cham, 2019, pp. 1469–1505, https://doi.org/10.1007/978-3-030-00069-1_31.
- [84] L.S. Dorobantu, S. Bhattacharjee, J.M. Foght, M.R. Gray, Analysis of Force Interactions between AFM Tips and Hydrophobic Bacteria Using DLVO Theory, Langmuir 25 (12) (2009) 6968–6976, https://doi.org/10.1021/la9001237.
- [85] M. Hayyan, M.A. Hashim, I.M. AlNashef, Superoxide Ion: Generation and Chemical Implications, Chem. Rev. 116 (5) (2016) 3029–3085, https://doi.org/10.1021/acs. chemrev.5b00407.
- [86] L.A.T.W. Asri, M. Crismaru, S. Roest, Y. Chen, O. Ivashenko, P. Rudolf, J.C. Tiller, H.C. van der Mei, T.J.A. Loontjens, H.J. Busscher, A. Shape-Adaptive, Antibacterial-Coating of Immobilized Quaternary-Ammonium Compounds Tethered on Hyperbranched Polyurea and its Mechanism of Action, Adv. Funct. Mater. 24 (3) (2014) 346–355. https://doi.org/10.1002/adfm.201301686.
- [87] A. Aliano, G. Cicero, H. Nili, N.G. Green, P. García-Sánchez, A. Ramos, A. Lenshof, T. Laurell, A. Qi, P. Chan, L. Yeo, J. Friend, M. Evander, T. Laurell, A. Lenshof, T. Laurell, J. Chen, J. Lacroix, P. Martin, H. Randriamahazaka, W.J.P. Barnes, B. W. Hoogenboom, K. Fukuzawa, H. Hölscher, H. Hölscher, A. Bottos, E. Astanina, L. Primo, F. Bussolino, X. Gao, V.-N. Phan, N.-T. Nguyen, C. Yang, P. Abgrall, F. G. Barth, P. Gurman, Y. Rosen, O. Auciello, C.J. Kähler, C. Cierpka, M. Rossi, B. Bhushan, M.L.B. Palacio, C.L. Dezelah, AFM in Liquids, in: B. Bhushan (Ed.), Encyclopedia of Nanotechnology, Springer Netherlands, Dordrecht, 2012, pp. 83–89.